Published in final edited form as:
Combust Flame. 2016 December ; 174: 16–24. doi:10.1016/j.combustflame.2016.09.004.

CO Emission from an Impinging Non-Premixed Flame

Y.C. Chien, **D. Escofet-Martin**, and **D. Dunn-Rankin**
Mechanical and Aerospace Engineering, University of California Irvine, Irvine, 92697. USA

Abstract

Carbon monoxide (CO) results from the incomplete oxidation of hydrocarbon fuels. While CO can be desirable in some syngas processes, it is a dangerous emission from fires, gas heaters, gas stoves, or furnaces where insufficient oxygen in the core reaction prevents complete oxidation of fuel to carbon dioxide and water, particularly when the reaction is interrupted by interaction with relatively cool solid boundaries. This research examines the physico-thermo-chemical processes responsible for carbon monoxide release from a small laminar non-premixed methane/air flame impinging on a nearby surface. We measure the changes in CO emission as correlated with variations in flame structure observed using planar laser induced fluorescence (PLIF of OH and 2-photon CO), and two-line OH PLIF thermometry, as a function of burner-to-plate distance. In particular, this work combines the use of OH and CO PLIF, and PLIF thermometry to describe the relative locations of the CO rich region, the peak heat release zone as indicated by chemiluminescence and OH gradients, and the extended oxidative zone in the impinging flames. The results show that CO release correlates strongly with stagnating flow-driven changes in the location and extent of high concentration regions of OH in surface-impinging diffusion flames.

Keywords

Carbon monoxide; Impinging flame; Diffusion flame; OH PLIF; CO PLIF

1. Introduction

There is a classic trade-off in combustion between the emission of primary pollutants (in particular, carbon monoxide versus the oxides of nitrogen, NOx). For example, low temperature combustion is known as a method to reduce NOx emissions and soot formation compared to high-temperature combustion but at the same time, low temperature combustion can generate excess carbon monoxide, CO, from incomplete reaction. Considering that it is not uncommon for CO concentrations within the rich core of nonpremixed flames to reach 5% [1], minimizing CO release from flames can be a critical design requirement for many combustion systems. Monitoring CO in the surroundings provides an alert to its dangerous presence and can prevent CO poisoning [2] but reducing the source of carbon monoxide benefits from an understanding of the incomplete combustion processes that lead to its release. CO from fuel rich premixed combustion is a natural consequence of the unavailability of oxidizing species. However, CO from nonpremixed flames can be more

Corresponding author. Tel.: +1-949-824-8745; fax: +1949-824-8585. Mailing address: 4200 Engineering gateway, University of California, Irvine, Irvine, CA, 92697, USA, chieny@uci.edu.

complicated because it can depend on mixing and transport factors as well as reaction rates. Incomplete combustion in nonpremixed systems such as fires, gas stoves, or gas heaters, produces CO when there is insufficient oxygen available in the core reaction zone to fully oxidize the products to carbon dioxide and water. The high CO concentration can then be kinetically frozen if it migrates to a relatively low temperature region, even if that region is oxygen rich. As a result CO emission is known to occur when a non-premixed flame burns near a relatively cool surface, which can create conditions near extinction (quenching) of the fire[3]. In addition, incomplete reaction from insufficient oxidizer can occur near relatively cool walls during intermittent or incipient extinguishment of the flame. Consequently, this research aims to describe the dominant features of carbon monoxide release from nonpremixed flames when those flames are in proximity of relatively cool solid surfaces.

Impinging flame studies have been carried on for decades with diverse focus of research interests associated with combustion near surfaces, though primarily with premixed flames. Viskanta tabulated different experimental impingement studies, including single or multiple turbulent jets, and compared the heat transfer results[4]. The work pointed out that the interaction of a flame jet with a surface will lead to chemical reaction and pollutant emission effects but that there is limited literature on single impinging flame jets. Foat et al. characterized turbulent propane premixed impinging flames with visualization over different burner geometries[5] and found that the final impinging flame pattern is dependent on many factors such as equivalence ratio, global stretch rate, initial ignition location and turbulence structure. Zuckerman et al. summarized and correlated a list of impingement experiments with Nusselt number and related parameters as a reference[6]. Baukal has a detailed survey of flame impingement measurement research which categorizes and organizes most studies up to 2010[7]. The main observation from all of these valuable comprehensive overviews of impinging jets and flames is that the majority of impinging flame experiments focus on turbulent heat transfer/heat flux with various burner configurations or fuels[8]. This is reasonable since many thermal processes rely on flame heating but the understanding of heat flux would benefit from insights regarding the flame characteristics as impinging surfaces are brought into the proximity of the reaction zone.

Combustion species such as CO, CO_2, NO, O_2 have been measured by gas chromatography (GC) in order to correlate with heat flux distributions in impinging flames[9,10]. Relatively fewer works directly measure and discuss how emissions are associated with the flame impingement. Mohr et al. compared CO, CO_2, O_2 and NOx emission for different equivalence ratios with Radial Jet Reattachment combustion (RJR) and co-axial nozzles[11]. The results, relevant to reducing emissions with jet design, show that CO concentration increases dramatically as the equivalence ratio goes from lean to rich. Mishra measured CO, NO, O_2 and CO_2 at two flow speeds (transition flow and turbulence) for premixed LPG (70% butane and 30% propane) impinging jet flames at three burner-to-plate distances[12]. The results showed that CO level can be related with Reynolds number as well as with equivalence ratio, indicating that both chemistry and the flow environment participate in the ultimate release of CO. Both of these emission studies used gas analyzers in the exhaust and did not resolve the spatial location of the species in the flame. Mann et al.[8] and Singh et al. [13] conducted CO measurements with laser induced florescence (LIF) for variations in impinging methane/air flames at lean, stoichiometric, and rich (over stationary transition

flow and turbulent regime) conditions. Their work aimed at examining flame quench in internal combustion engines, and they included temperature and heat flux measurements, and compared their findings to simulation. Their results showed that higher CO mole fractions are present at lower temperatures in the lean premixed flame than in the stoichiometric flame for the same heat flux over enthalpy loss near the wall. All of the above-mentioned studies examined CO emission under premixed and partially premixed flame conditions, and they all had a minimum flow speed threshold because for premixed flames a minimum speed is needed to avoid flashback. The current work focuses on laminar nonpremixed flames.

One of the key motivations for the current study were the measurements of Weinberg, et al. showing CO release from a small diffusion flame as a quenching surface was brought into its proximity[1]. By relating surface proximity to CO release, the study showed that electrical detection of the flame-to-surface distance could be used to identify incipient quenching and CO release. They also postulated that the source of CO release from impinging diffusion flames was the high concentration of partially oxidized fuel inside the flame envelope that avoids the final oxidation step. While this postulate seems obvious, it does not alone identify how changes to the reaction zone structure generated by the quenching surface were responsible for the failure of complete oxidation. It is not clear, for example, which aspect of the change was dominant: physical (e.g., changes in flow time caused by boundary layers), chemical (e.g., changes in the relative concentration of critical reactants), or thermal (changes in temperature related to heat losses to the wall). The current work helps clarify these various aspects by relating experimentally the flame structure to CO emission when a quenching surface gradually moves close to a small diffusion flame.

This paper provides a fundamental and comprehensive experimental evaluation of a small methane diffusion flame jet flowing at low Reynolds number (approximately 50) and impinging on a relatively cool downstream surface. It contributes to the body of knowledge involving laminar impinging flames and it provides detailed information regarding the source of carbon monoxide emission with varying impinging distance. In order to help elucidate some of the processes that might account for the CO emission from an impinging non-premixed flame, we provide schlieren images of the impinging flame and infrared thermal images of the impinging plate to confirm its laminar flow nature and the overall thermal profile at the surface. We present natural flame images, which represents CH* and OH* chemiluminescence to show the reaction zone; OH planar laser induced fluorescence (PLIF) images combined with carbon monoxide two-photon PLIF images demonstrate that OH is a key reactant for diffusion flames particularly as the oxidant for carbon monoxide to CO_2 [14] and confirm the relationship between the location of CO and the effects of flame impingement. Finally, we include two-line OH PLIF thermometry findings to indicate thermal effects of the impingement plate.

2. Experimental

2.1 Burner and flame

The experiments are conducted with a coflow burner and a 2 mm thick stainless steel plate progressively lowered toward the burner surface so that it gradually quenches the flame [15].

The system setup is shown in Figure 1. The stainless steel coflow burner is 13 cm tall and has a 4 cm outer diameter. At the exit, the burner has a 2 mm inner diameter center tube carrying methane fuel, and air is provided separately through a concentric outer ring. The burner is modeled after the coflow burner used in a wide range of lifted non-premixed flame studies by the group at Yale University [16,17]. The annulus is designed to have a uniform air flow distribution at the exit after it passes through a bed of beads and a honeycomb mesh close to the exit. Inside the burner, the length of the tube is sufficient to ensure fully developed flow at the exit. Hot wire anemometry scans across the burner exit under cold flow conditions confirm this steady fully developed condition. Further details on the burner are provided in [15,18]. The metal plate used as the quenching surface is 10.2 by 10.2 cm (4 by 4 inches) square. It is connected onto a vertical-axial translation stage. The diffusion flame used for this work has flow rates equivalent to a constant nominal speed of 20 cm/s for both methane and air at the burner exit as laminar flow.

Figure 2 shows the natural flame image (mostly CH* chemiluminescence) as the impinging plate is progressively lowered towards the flame. H/D represents plate height to the nozzle diameter as a dimensionless scale. At H/D 5.5 the visible flame is not affected by the impinging plate; at H/D 4.5 the flame tip begins to open with the interference from the plate. Schlieren images (an example image appears in Figure 3 highlighting the main features) show steady laminar flow fields, with a typical stagnation point flow boundary layer shape extending radially outward on the plate to its edge. The focused schlieren image is created with a typical Z-type two-mirror system illuminated with a continuous Xenon light source (Hamamatsu Model E7536). The knife-edge was aligned parallel to the quenching plate in order to emphasize the gradients normal to that direction. At the edge of the plate the rising thermal plume produces some recirculation zones on the backside of the plate but these flows do not affect the core stagnation flow region. Plate temperature is monitored with an infrared camera situated directly above the impinging plate at normal incidence to avoid complications associated with Lambert’s cosine law. The camera (FLIR SC620) measures radiative emission in the range from 7.5 to 13 microns and the plate is coated with black paint to produce a nominally black body radiant surface. The detailed experiment and process has been described and presented [15] if further details are needed. One example thermal image, calibrated by a thermocouple measurement at a single point, Figure 4, shows that the impinging plate (the rectangular area) is much larger than the flame (the centered hot area). The region outside of the impinging plate (dark blue) is the optical table at room temperature. The temperature is distributed concentrically outward from high to low, with the maximum temperature located at the center. The high thermal conductivity of the plate, coupled with its large size, assures that integrated heat flux loss impact of the plate is independent of impingement distance even without external temperature control of the plate. Temperature distributions recorded at each impinging height confirm that the small changes in the plate temperature are inconsequential and do not affect the flame quenching behavior.

2.2 Carbon monoxide release

The overall carbon monoxide emission from the flame is measured with a portable combustion analyzer (TSI CA-CALC 6200) that aspirates gas from inside an acrylic chamber enclosing the burner at a low (to prevent flow disturbance in the chamber) and

fixed flow rate. The generated exhaust gases from the flame, including the CO from quenching, fills the chamber and mixes with the existing and coflow air to yield a gradually increasing concentration in the chamber. As in the classical tank dilution problem, the mixing process produces a time-exponential approach to a steady state concentration. The acrylic chamber was designed to create a steady environment for the experiment and to diminish the external influence of air currents on the small flame. For each case of carbon monoxide emission measurement, the chamber is first flushed with air. The flame is then operated for four minutes before the CO measurement is taken. The decay rate and generation rate have been considered and analyzed to show that for the conditions of our experiments essential steady state is reached after 2 minutes [15]. This global CO measurement is very stable, reproducible, and accurate but it does not necessarily reflect a relevant absolute concentration since the dilution level is not explicitly controlled (it occurs naturally in the chamber). However, we are concerned with relative effects of plate impingement so the results are provided in a form that is normalized to the CO concentration achieved in the chamber from a flame unaffected by the quenching plate.

2.3 OH PLIF

The OH PLIF technique has provided valuable information from flames for many years [19,20]. Our PLIF measurements follow generally recommended practice [19,21] and are conducted by pumping OH at 282.0 nm in the A-X(1,0) band and detecting fluorescence in the A-X(0,0), (1,1) band. The set up used for this specific realization of the technique includes a 10 Hz Surelite III Nd:YAG laser, followed by a Vista dye laser using (Rhodamine 590 dye dissolved in methanol) and a wavelength extender. The sheet forming optics comprises a spherical lens plus a cylindrical lens, forming a sheet with a height of 3 cm. The pulse energy was kept below 4mJ where it could be observed experimentally that the transitions were linear. The linearity of the signal was checked by comparing the overall integrated signal of the fluorescence images from the camera with the average energy from the laser used for the images. The transition selected from the A-X (1,0) is the R1(10) around 283 nm. The temperature sensitivity of the transition selected has been compensated for by using the two-dimensional thermal information from the ratio of the transitions R1(3) and R1(10) (explained in the next subsection).

The fluorescing light was collected using an EM-ICCD PIMAX-4. The filter used (Semrock FF01-320/40-25) offers very good transmissivity (70%) to collect the light from the A-X(0,0) transition. The images were taken using a 300 ns gate, which is long enough to collect the fully integrated signal of the fluorescence and short enough to suppress the background chemiluminescence. Absorption through the flame is negligible; this is because the inner diameter of the burner is only 2 mm, and there is not enough OH concentration to make absorption relevant. 200 images were collected for every transition and position. After taking the fluorescence images for each transition, the flame was moved away, putting instead a quartz dye cell with a diluted mixture of methanol with dye, in order to accurately correct for intensity variations across the laser sheet. This correction procedure was repeated for all the positions and transitions. Figure 5 shows the entire OH PLIF setup. In addition using the same collection optics setup chemiluminescence images were collected for each position, see Figure 6.

2.4 Two-line OH PLIF thermometry

The basis for two-line OH temperature PLIF has been described in the past[22–24], and only a brief description is given here. The linear LIF signal S is a function of:

$$S=\eta I N_t \left(2J^{''}+1\right) \exp(\frac{-E}{kT}) BG\Phi(T,J^{'})$$

Where η is the optical detection efficiency, I intensity of the laser power, $J^{''}$ the rotational quantum number of the excited ground state and $J^{'}$ the rotational quantum number of the excited upper electronic state, N_t is the total number of OH molecules, E is the energy of the ground state, B is the absorption Einstein coefficient, G is the spectral overlap integral between laser and molecular absorption profile, and Φ is the fluorescence quantum yield. Assuming similar collection efficiencies due to using the same camera, camera filter and the same laser setup for two different transitions (1 and 2), we can obtain:

$$\frac{S_1}{S_2}=\frac{I_1}{I_2}\frac{(2J_1''+1)}{(2J_2''+1)}\exp(\frac{-(E_1-E_2)}{kT})\frac{B_1}{B_2}\frac{G_1}{G_2}\frac{\Phi_1(T,J^{'})}{\Phi_2(T,J^{'})}$$

The ratio S_1/S_2 at every pixel of the camera is a function of several constants, temperature, laser intensity, both overlap integrals, and the ratio of both quantum fluorescent yields. The spectral overlap between laser profile and absorption line profile is assumed to be the same for both transitions, which is a source of a small systematic error, even though the laser profile is very similar for both transitions. Since we are working with the same laser setup in a narrow range of wavelength, Doppler and collisional effects depend on the rotational quantum number, but in the calculations we assume that line broadening for the two transitions is similar; this is not a significant source of error and it is one of the easiest assumptions to relax to improve the measurements using a theoretical model to adjust the change in spectral absorption profile. The quantum fluorescence yield ratio is difficult to determine because of the complex behavior of the collisions and energy exchange through vibrational and rotational energy transfer (VET and RET) in the nonequilibrium upper electronic state. From a theoretical standpoint the best way to solve that problem, as has been proposed, is using two transitions that share a common upper state[25]. In that way the ratio of fluorescence yield would be unity. Unfortunately, this ideal situation is not possible for our case because the exponential dependence of the energy difference in the ground state (for the OH molecule) makes this energy difference so small that the sensitivity of the measurement becomes very low, reducing dramatically the signal to noise ratio of the measurement. The most common technique for finding the ratio is to do so experimentally by using an alternative temperature measurement for a certain position of the flame, and then using that measurement to calculate this ratio[24]. This last method has not been used in this case because of the spatial resolution of the alternative method (e.g., thermocouple) would be far worse than the one offered from the OH two-line PLIF, making it unacceptably approximate for our small spatial scales due to averaging and the high gradients present in the flame. For that reason we assumed rapid rotational thermal stabilization in the upper electronic state that would lead to a ratio that is approximately unity[26]. This assumption

produces a systematic error in the measurements but again the error can be bounded as relatively small based on expected deviations from the unity fluorescence yield ratio. The decision of the transition pair has taken into account several factors: transition strength, transition isolation from neighboring transitions, and maximum energy difference in the ground state with no interference from surrounding species, the line pair used is R1(3) with R1(10). The specified equipment for the thermometry measurements is the same as is used for the OH PLIF. In addition, vignetting is known to be a problem for the measurements close to a plate[8,13]; being that the plate and the burner surface are much larger than the flame, the effects of vignetting are greatly reduced for each picture. A small aperture was used in order to reduce the impact over the images at lower impinging plate heights. Further comparison of relative intensity for different impingement plate heights will be affected by the vignetting that decreases the overall solid angle collected for the smallest H/D ratios.

2.5 CO two-photon PLIF

The basis for two-photon CO fluorescence has been described in the literature [27,28], and only a brief review is given here. The two-photon CO signal S depends on a wide range of parameters, and is given by:

$$S \propto \frac{N_t F_{j''} W^{2v}}{Q+A+P+\Gamma}$$

N_t is the total number of CO molecules in the volume; $F_{j''}$ is the fractional population of CO in the pumped ground state, which is a function of temperature; W^{2v} is the two-photon absorption rate coefficient, which is a function of the intensity squared as well as of the absorption cross section and the intensity of the laser profile; Q represents the quenching, which is a function of collisional partners, temperature and pressure A is the spontaneous emission from the excited state; P is predissociation, and Γ is the single-photon ionization rate coefficient, which is a linear function of intensity. Although complex, many of these values can be determined, at least for relative conditions, permitting CO fluorescence to provide a clear qualitative view of the spatial distribution of this important molecule.

In order to find a more detailed behavior of the signal as a function of wavelength and temperature, a simulation of the Q branch of the $B^1\Sigma^+ \leftarrow\leftarrow X\Sigma^+$ transition for CO has been accomplished, following a procedure similar to that described in [29]. The rotational energies are calculated using the spectroscopic constants from [30,31]. The line positions only include $\Delta J = 0$, the Q branch, which is the strongest. For the line strength, the two-photon absorption cross-sections are taken from [32]. The excitation line shape is assumed to be Gaussian with a FWHM of 0.8 cm^{-1}. The Honl-London factors for linear polarization are given by [33]. The transition line shape is calculated with a Voigt profile, combining the Doppler broadening and pressure broadening. The population has been assumed to follow a Boltzmann distribution, and the two photon cross section is assumed to be constant through all the rotational transitions; at high energy fluence, as studied in [34], the signal becomes dominated by the ionization effect, and in this regime the signal becomes approximately linear with laser intensity; the ionization cross section is assumed to be constant through the range of wavelengths studied.

The wavelength chosen for the experiment is 230.034; the wavelength was monitored and calibrated with a Xenon lamp and a 1 meter spectrometer. This wavelength coincides with the high intensity region of Figure 7; this wavelength belongs to the transitions in the Q branch with a rotational quantum number around J=11. As shown in Figure 8, the shift of populations in the lower level means that the fluorescence signal at 800 K is about 15% higher with respect to the signal at 1200 K, and the signal at 1700 K is about 15 % lower than the signal at 1200 K. It is possible to use higher J value transitions to reduce this temperature dependence but this comes at the expense of reduced signal strength. Our goal in this work was a planar measurement over a relatively large spatial area and so we chose the higher signal strength and accepted the concomitant increase in correctable temperature dependence.

The cylindrical lens was selected to be 100 mm focal length in order to stay in the linear regime of the CO fluorescence, that is, the regime where the CO ionization dominates. The beam waist is calculated to be about 50 μm in thickness, and the average power density is approximately 0.5 GW/cm^2. The laser sheet limits the measurement region to the 4 mm closest to the plate, as shown in Figure 9. The laser power density is high enough to ensure that ionization dominates the depopulation of the upper state, giving an approximately linear behavior with intensity for atmospheric pressure conditions. Several photochemical effects affect the fluorescence signal, including C_2 formation, CO ionization, CO_2 dissociation, and CO dissociation. The C_2 signal overlaps spatially, spectrally and temporally to some degree with the CO fluorescence signal. Using a long pass filter at 300 nm shows that the signal coming from C_2 is one order of magnitude higher than the CO signal (using 100 ns integration gate) for the studied flame; however, using a filter at 486 nm, and following similar procedures as described in [8], reduces the C_2 signal to a negligible level. CO dissociation is insignificant at the pressure and energy density values for the experiment. As described earlier, CO ionization is very important and dominates quenching in the depopulation of the excited state. CO_2 dissociation has a strong dependence on temperature, and under 1400K the process is weak enough that it has a relatively small contribution. On the other hand, in the high temperature regions where CO_2 dissociation can be important, the CO concentration is generally high enough to keep the relative contribution of this dissociative interference small. We concentrate on the low temperature region in any case as we are studying the zone close to the impingement plate.

3. Results and discussion

To determine the effects of a nearby surface on CO levels, the downstream plate is moved to different heights above the burner. As has been described in the literature, the absolute distance between the burner and the plate is not as important as the plate’s location relative to the flame tip. In the case of jet impingement, the relevant distance is related to the jet momentum since the stagnation zone affects the downstream region only. Consequently, we provide the downstream plate in units relative to the jet diameter (H/D), as is customary in the impingement literature Based on the burner jet dimension of 2 mm, however, it is straightforward to convert these normalized values to physical distances.

Figure 10 shows the steady CO release as the plate progressively moves toward the burner. It is clear that the carbon monoxide level increases rapidly and steadily once the plate approaches the flame tip. The CO concentration is given in scaled units relative to the unimpeded conditions that prevail beyond plate distances of 27 mm (H/D 13.5). The absolute value of CO concentration at this baseline condition is around 17.5 ppm in a chamber after dilution with the coflow air. Because of flame quenching, the CO concentration grows rapidly as the plate distance drops below H/D of 4.5, exceeding ten times the baseline value as H/D decreases below 3 and more than 30 times the baseline value at the smallest plate distance before extinction.

To better understand the gross and subtle relationships between plate proximity and CO emission, we explore changes in flame structure associated with the influence of the impingement plate. Detailed experimental results in the literature for steady coflow methane/air diffusion flames show that the high CO concentration area is located on the fuel side of the high temperature reaction region and on the fuel side of the OH zone. The rate of differential diffusion maintains the stability of the laminar flame[35]. In an unperturbed flame, most of this CO is oxidized to CO_2 and only a small fraction escapes to the environment. For the case of the impinging flame, heat is lost to the plate, which affects the chemistry, and the flame and flow field change shape, which affects the transport. One question is which of these has the greatest impact on CO release.

Research has shown that OH fluorescence can be employed as a marker for the reaction zone [19,36,37], and it has been shown that the predominant influences on CO in hydrocarbon flames at similar velocities and compositions to ours are the reactions[38] [14]:

$$\mathrm{H}+\mathrm{O}_2 \rightarrow \mathrm{OH}+\mathrm{O} \quad (1)$$

$$\mathrm{CO}+\mathrm{OH} \rightarrow \mathrm{CO}_2+\mathrm{H} \quad (2)$$

$$\mathrm{CH}_4+\mathrm{OH} \rightarrow \mathrm{CH}_3+\mathrm{H}_2\mathrm{O} \quad (3)$$

$$\mathrm{CH}_3+\mathrm{O}_2 \rightarrow \mathrm{H}_2\mathrm{CO}+\mathrm{OH} \quad (4)$$

Carbon monoxide oxidation depends heavily on hydroxyl radicals to form carbon dioxide. Reaction (3) in the high-temperature oxidation of methane/air flames consumes hydroxyl faster than does the carbon monoxide oxidation reaction (2). This competition for OH leads to a CO accumulation [14]. Significant emission occurs if this accumulated CO is not oxidized in another region of the flame. It is also important to recognize that the formation of OH requires oxygen in reactions (1) and (4) so it is created in the outer layers of the reaction zone. Smyth et al. measured the distribution of carbon monoxide and marked the

OH boundary of a diffusion flame in a Wolfhard-Parker slot burner during their soot research [39]. They showed that the location of the peak carbon monoxide emissions is inside the OH boundary and the overall carbon monoxide is inward but attached to the OH region. Detailed CO profiles and contour maps have been presented for different laminar diffusion combustion systems [40–43]. In particular, Weinberg et al. show that the surprisingly high level of CO along the axis in small diffusion flames (even in the absence of partial premixing) is due to diffusion from zones close to the reaction sheet[42]. All these results suggest that the distribution of OH can provide insight into the CO oxidation effects with quenching distance.

Figure 11 is a comprehensive data record of the current work. From left to right, it shows OH PLIF, the natural flame chemiluminescence, two-photon CO PLIF, schlieren images, and IR images of the plate. From top to bottom, the impinging plate is progressively moved closer to the flame at the normalized plate-to-burner distance H/D. The schlieren image (2nd column from the right) shows that the overall experiment conditions are within the steady stagnation laminar flow regime without perturbation. The recorded infrared thermal image (rightmost images) assures for all the experiment impingement conditions that the impinging plate is a relatively large sink for the heat from the flame. The outer regime of the plate remains around 350 Kelvin (about 70 Celsius) for all the plate heights. Notice that due to the FLIR camera performance, all the images are scaled at their own maximum temperature, which varies less than 10% between H/D of 5.5 and 1.5. Part of the thermal uniformity is due to the fact that as the plate gets closer to the flame the impinging heat transfer zone is spread wider, reducing the peak value.

At H/D 5.5, the OH PLIF (leftmost column) semi-quantitative image shows that hydroxyl is strongly surrounding the flame reaction zone and is gathered as a cloud on top of the flame. At this impinging plate location, where the flame has not been interfered with, there is no CO observed (the third column image). At H/D 4.5, where the flame tip begins to open, the OH cloud near the plate starts separating and CO is imaged right on top of the flame where the least hydroxyl is distributed. When the impinging plate is lowered to H/D 3.5, the OH is sitting to the side at the two wings of the opened flame; CO is gathering near the impinging surface and escaping along the plate from within the flame. The natural flame and the OH images show that the flame is being opened even wider at H/D 2.5. In this condition the CO forms a V shape with the flame geometry and is stronger near the surface. A similar sequence of observations can be seen at H/D 1.5; at this location the two wings of the OH have changed their orientation completely as they now face outside. The CO distributes even more strongly and wider along the impinging surface, especially at the two sides right on top of the OH cloud.

There have been some suggestions in the literature that the plate cools the flame, and that it is this reduction in temperature that leads to the incomplete combustion that produces CO. However, as shown in Figure 12, the two-line OH PLIF temperature measurements of flames near a quenching plate show a consistent OH temperature distribution even with the plate-to-burner distance decrease. For all the conditions, the higher temperature region is located at the inner side around the reaction zone. Overall peak temperatures range between 1600–1700K. Figure 12 shows that the OH cloud has a similar temperature distribution, with its

maximum at the reaction front and decreasing toward the surroundings, independent of the plate-to-burner distance. The only difference is that the flame geometry is perturbed and opened up by the impinging plate so that the reaction is opened and facing upward; this phenomenon can be confirmed with the IR images of the impinging plate (Figure 11, right). The plate temperature distribution and gradients are similar even as the H/D and flame shape changes fairly dramatically. This consistent OH temperature distribution with the plate-to-burner distance decrease implies that the plate does not reduce the peak flame temperature but rather, with the plate getting closer to the burner, interrupts the flame by creating a stagnating flow that changes substantially the reaction zone geometry.

The fact that the velocities were kept low so that the flow behaves as a laminar stagnation flow gives one reason for the overall oxidation decrease of the CO molecule as being due to the lower OH concentration and shorter residence time for reaction through the OH layer as the plate approaches the burner. The tip of the OH radical zone opens because the plate splits the flow and brings intermediate products from the center fuel region out along the impinging surface. Other work mentions that the OH radical is not expected to exist below 1000K [44], which is why the OH reaction zone does not develop further along the impinging surface and decays with residence time decrease instead.

4. Conclusion

This paper provides experimental evidence for the relationship between CO emission and small nonpremixed flames impinging on a relatively cool surface. The main contributions of this research are: understanding carbon monoxide release with plate location and the role of the OH distribution. It describes particularly the spatial relationship between reaction zone and heat release zone with quenching in small non-premixed flames, and how the relationship can affect CO release. OH location and concentration during flame quenching correlates strongly with carbon monoxide release. In particular, the study shows that the primary reason for CO release from these small flames is that the stagnating flow influences the relative transport path of the key reactive intermediates responsible for CO oxidation. Allowing the core CO a path to the environment in the relatively cool gas layer along the plate surface bypasses the reactive OH cloud and permits its escape. Additional investigations will explore similar questions with partially premixed rich flames similar to those used more commonly in domestic burner applications.

Acknowledgments

This work is supported by NASA’s ISS Research Project via agreement NNX11AP42A with Dennis Stocker as Technical Monitor. The authors would also like to acknowledge the contributions to the experiment of Koji Yamashita from Aoyama Gakuin University.

References

1. Weinberg FJ, Dunn-Rankin D, Carleton FB, Karnani S, Markides C, Zhai M. Electrical aspects of flame quenching. Proceedings of the Combustion Institute. 2013; 34:3295–3301. DOI: 10.1016/j.proci.2012.07.007
2. U. EPA, US Environmental Protection Agency. (n.d.). http://www.epa.gov/ (accessed October 1, 2015)

3. Baukal, CE. Industrial Combustion Testing. 1st. CRC Press; 2010.
4. Viskanta R. Heat transfer to impinging isothermal gas and flame jets. Experimental Thermal and Fluid Science. 1993; 6:111–134. DOI: 10.1016/0894-1777(93)90022-B
5. Foat T, Yap KP, Zhang Y. The visualization and mapping of turbulent premixed impinging flames. Combustion and Flame. 2001; 125:839–851. DOI: 10.1016/S0010-2180(00)00238-8
6. Zuckerman N, Lior N. Jet Impingement Heat Transfer: Physics, Correlations, and Numerical Modeling, Advances in Heat Transfer. 2006; 39:565–631.
7. Baukal, CE. Industrial Combustion Testing. 1st. CRC Press; 2010.
8. Mann M, Jainski C, Euler M, Böhm B, Dreizler A. Transient flame–wall interactions: Experimental analysis using spectroscopic temperature and CO concentration measurements. Combustion and Flame. 2014; 161:2371–2386. DOI: 10.1016/j.combustflame.2014.02.008
9. Dong LL, Leung CW, Cheung CS. Combustion optimization of a slot flame jet impingement system. Journal of the Institute of Energy. 2003; 76:80–88.
10. Sze LK, Cheung CS, Leung CW. Temperature distribution and heat transfer characteristics of an inverse diffusion flame with circumferentially arranged fuel ports. International Journal of Heat and Mass Transfer. 2004; 47:3119–3129. DOI: 10.1016/j.ijheatmasstransfer.2004.02.015
11. Mohr JW, Seyed-Yagoobi J, Page RH. Combustion measurements from an impinging Radial Jet Reattachment flame. Combustion and Flame. 1996; 106:69–80. DOI: 10.1016/0010-2180(95)00246-4
12. Mishra DP. Emission studies of impinging premixed flames. Fuel. 2004; 83:1743–1748. DOI: 10.1016/j.fuel.2004.02.019
13. Singh A, Mann M, Kissel T, Brübach J, Dreizler A. Simultaneous Measurements of Temperature and CO Concentration in Stagnation Stabilized Flames. Flow Turbulence Combust. 2012; 90:723–739. DOI: 10.1007/s10494-011-9384-6
14. Glassman, I. Combustion. Academic Press; 1997.
15. Chien, YC. Electrical Aspects of Impinging Flames. UNIVERSITY OF CALIFORNIA; IRVINE: 2015. http://gradworks.umi.com/36/82/3682710.html (accessed April 14, 2016)
16. Dworkin S, Schaffer A, Connelly B, Long M, Smooke M, Puccio M, Mcandrew B, Miller J. Measurements and calculations of formaldehyde concentrations in a methane/N2/air, non-premixed flame: Implications for heat release rate. Proceedings of the Combustion Institute. 2009; 32:1311–1318. DOI: 10.1016/j.proci.2008.05.083
17. Mohammed RK, Tanoff MA, Smooke MD, Schaffer AM, Long MB. Computational and experimental study of a forced, timevarying, axisymmetric, laminar diffusion flame. Symposium (International) on Combustion. 1998; 27:693–702. DOI: 10.1016/S0082-0784(98)80462-1
18. Karnani S, Dunn-Rankin D, Takahashi F, Yuan ZG, Stocker D. Simulating Gravity in Microgravity Combustion Using Electric Fields. Combustion Science and Technology. 2012; 184:1891–1902. DOI: 10.1080/00102202.2012.694740
19. Hanson RK. Combustion diagnostics: Planar imaging techniques. Symposium (International) on Combustion. 1988; 21:1677–1691. DOI: 10.1016/S0082-0784(88)80401-6
20. Kaiser SA, Long MB. Quantitative planar laser-induced fluorescence of naphthalenes as fuel tracers. Proceedings of the Combustion Institute. 2005; 30:1555–1563. DOI: 10.1016/j.proci.2004.08.263
21. Schmidt JB, Ganguly BN. Point-to-plane pulsed discharge initiated flame structure modification in propane–air flame. Journal of Physics D: Applied Physics. 2012; 45:045203.doi: 10.1088/0022-3727/45/4/045203
22. Eckbreth, AC. Laser Diagnostics for Combustion Temperature and Species. CRC Press; 1996.
23. KoHse-HoingHaus. Applied Combustion Diagnostics. CRC Press; 2002.
24. Seitzman JM, Hanson RK, DeBarber PA, Hess CF. Application of quantitative two-line OH planar laser-induced fluorescence for temporally resolved planar thermometry in reacting flows. Applied Optics. 1994; 33:4000.doi: 10.1364/AO.33.004000 [PubMed: 20935747]
25. Cattolica R. OH rotational temperature from two-line laser-excited fluorescence. Applied Optics. 1981; 20:1156.doi: 10.1364/AO.20.001156 [PubMed: 20309279]

26. Giezendanner-Thoben R, Meier U, Meier W, Heinze J, Aigner M. Phase-locked two-line OH planar laser-induced fluorescence thermometry in a pulsating gas turbine model combustor at atmospheric pressure. Applied Optics. 2005; 44:6565.doi: 10.1364/AO.44.006565 [PubMed: 16270545]
27. Haumann J, Seitzman JM, Hanson RK. Two-photon digital imaging of CO in combustion flows using planar laser-induced fluorescence. Opt Lett OL. 1986; 11:776–778. DOI: 10.1364/OL.11.000776
28. Seitzman JM, Haumann J, Hanson RK. Quantitative two-photon LIF imaging of carbon monoxide in combustion gases. Appl Opt AO. 1987; 26:2892–2899. DOI: 10.1364/AO.26.002892
29. Carrivain, O., Orain, M., Dorval, N., Morin, C., Legros, G. Spectroscopic studies of carbon monoxide: application for detection in flames. Hungary. 2015. http://www.ecm2015.hu/papers/P3-11.pdf
30. Varberg TD, Evenson KM. Accurate far-infrared rotational frequencies of carbon monoxide. The Astrophysical Journal. 1992; 385:763–765. DOI: 10.1086/170983
31. Amiot C, Roncin JY, Verges J. First observation of the CO E 1 Π to B 1 Σ + and C 1 Σ + to B 1 Σ + band systems. Predissociation in the E 1 Π(v=0) level. J Phys B: At Mol Phys. 1986; 19:L19.doi: 10.1088/0022-3700/19/1/004
32. Rosa MDD, Farrow RL. Cross sections of photoionization and ac Stark shift measured from Doppler-free B ← X(0,0) excitation spectra of CO. J Opt Soc Am B JOSAB. 1999; 16:861–870. DOI: 10.1364/JOSAB.16.000861
33. Bray RG, Hochstrasser RM. Two-photon absorption by rotating diatomic molecules. Molecular Physics. 1976; 31:1199–1211. DOI: 10.1080/00268977600100931
34. Nefedov AP, Sinel'shchikov VA, Usachev AD, Zobnin AV. Photochemical Effect in Two-Photon Laser-Induced Fluorescence Detection of Carbon Monoxide in Hydrocarbon Flames. Applied Optics. 1998; 37:7729.doi: 10.1364/AO.37.007729 [PubMed: 18301610]
35. Skaggs RR, Miller JH. Tunable diode laser absorption measurements of carbon monoxide and temperature in a time-varying, methane/air, non-premixed flame. Symposium (International) on Combustion. 1996; 26:1181–1188. DOI: 10.1016/S0082-0784(96)80334-1
36. CATTOLICA RJ, VOSEN SR. Two-Dimensional Fluorescence Imaging of a Flame-Vortex Interaction. Combustion Science and Technology. 1986; 48:77–87. DOI: 10.1080/00102208608923885
37. Smyth KC, Harrington JE, Johnsson EL, Pitts WM. Greatly enhanced soot scattering in flickering CH4/Air diffusion flames. Combustion and Flame. 1993; 95:229–239. DOI: 10.1016/0010-2180(93)90064-A
38. Warnatz J. The structure of laminar alkane-, alkene-, and acetylene flames. Symposium (International) on Combustion. 1981; 18:369–384. DOI: 10.1016/S0082-0784(81)80042-2
39. Smyth KC, Miller JH, Dorfman RC, Mallard WG, Santoro RJ. Soot inception in a methane/air diffusion flame as characterized by detailed species profiles. Combustion and Flame. 1985; 62:157–181. DOI: 10.1016/0010-2180(85)90143-9
40. Mitchell RE, Sarofim AF, Clomburg LA. Experimental and numerical investigation of confined laminar diffusion flames. Combustion and Flame. 1980; 37:227–244. DOI: 10.1016/0010-2180(80)90092-9
41. Miller JH, Elreedy S, Ahvazi B, Woldu F, Hassanzadeh P. Tunable diode-laser measurement of carbon monoxide concentration and temperature in a laminar methane–air diffusion flame. Appl Opt AO. 1993; 32:6082–6089. DOI: 10.1364/AO.32.006082
42. Weinberg F, Carleton F, Houdmont R, Dunn-Rankin D, Karnani S. Syngas formation in methane flames and carbon monoxide release during quenching. Combustion and Flame. 2011; 158:273–280. DOI: 10.1016/j.combustflame.2010.08.016
43. Weinberg FJ, Dunn-Rankin D, Carleton FB, Karnani S, Markides C, Zhai M. Electrical aspects of flame quenching. Proceedings of the Combustion Institute. 2013; 34:3295–3301. DOI: 10.1016/j.proci.2012.07.007
44. McMillin BK, Seitzman JM, Hanson RK. Comparison of NO and OH planar fluorescence temperature measurements in scramjet model flowfield. AIAA Journal. 1994; 32:1945–1952. DOI: 10.2514/3.12237

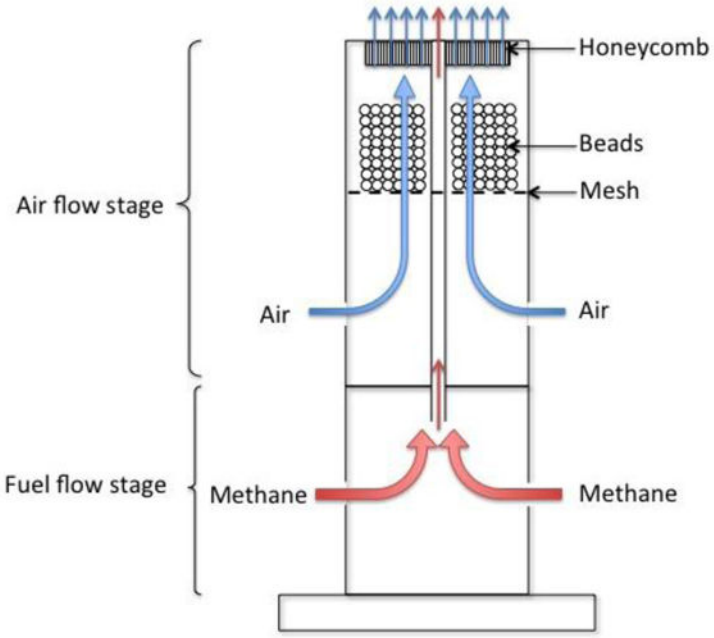

(a)

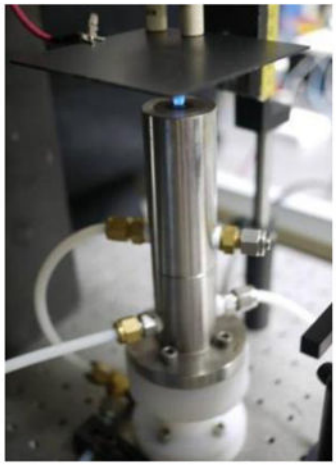

(b)

Figure 1.

Schematic diagram of the experiment. (a) Side view schematic of the coflow burner and gas flow. (b) A photograph of the coflow burner in operation.

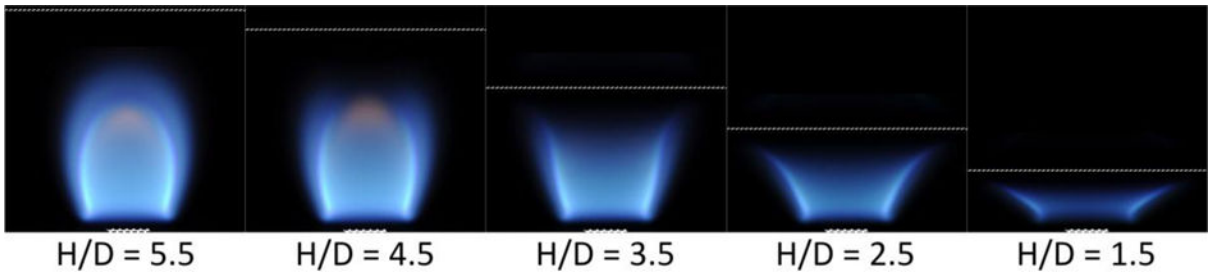

Figure 2.
Experimental conditions. The bottom line of the image is aligned with the level of the jet exit where the inner diameter of the 2 mm diameter methane fuel tube is marked.

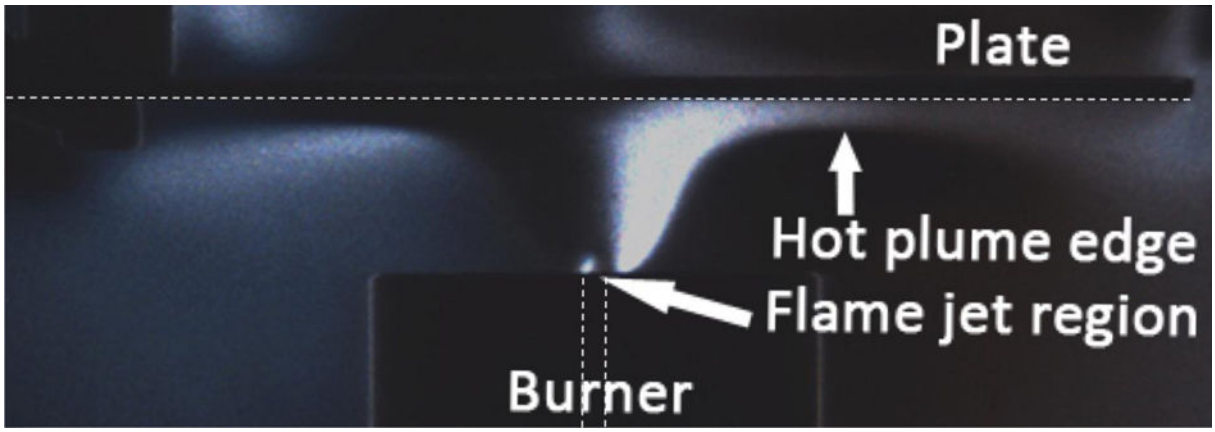

Figure 3.
Schlieren image of the flow field with at H/D = 4.5.

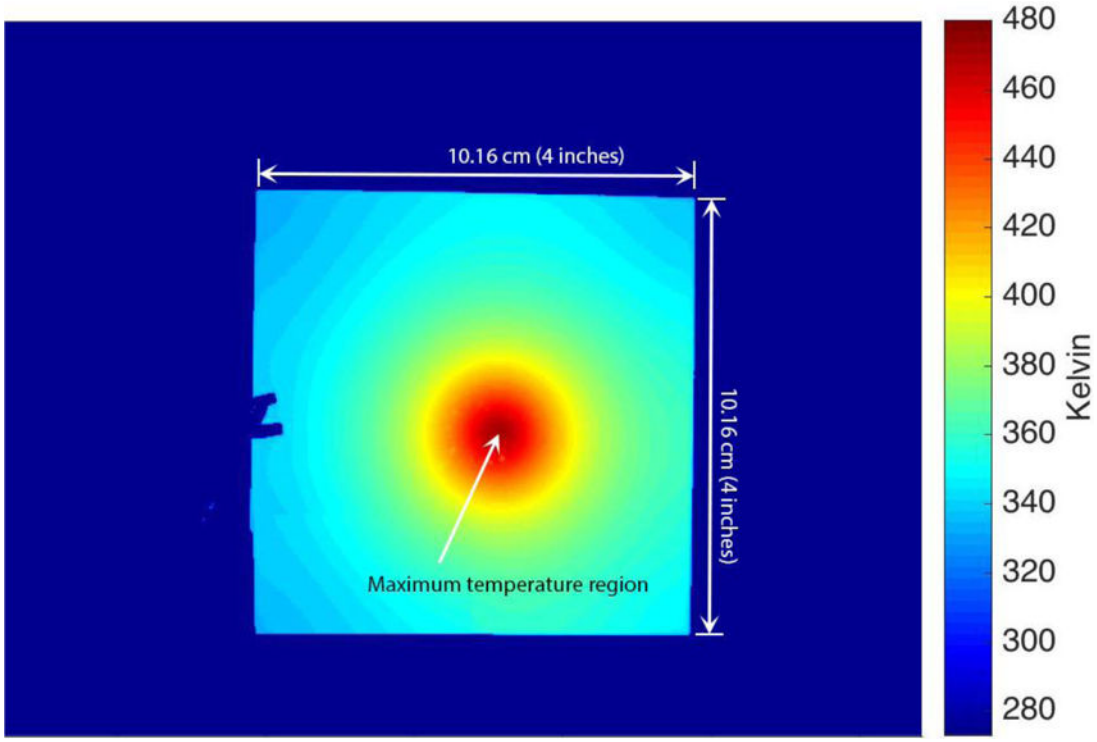

Figure 4.

An example Infrared image of the impinging plate; the maximum temperature is located at the center of the plate. The flame condition is at H/D 4.5.

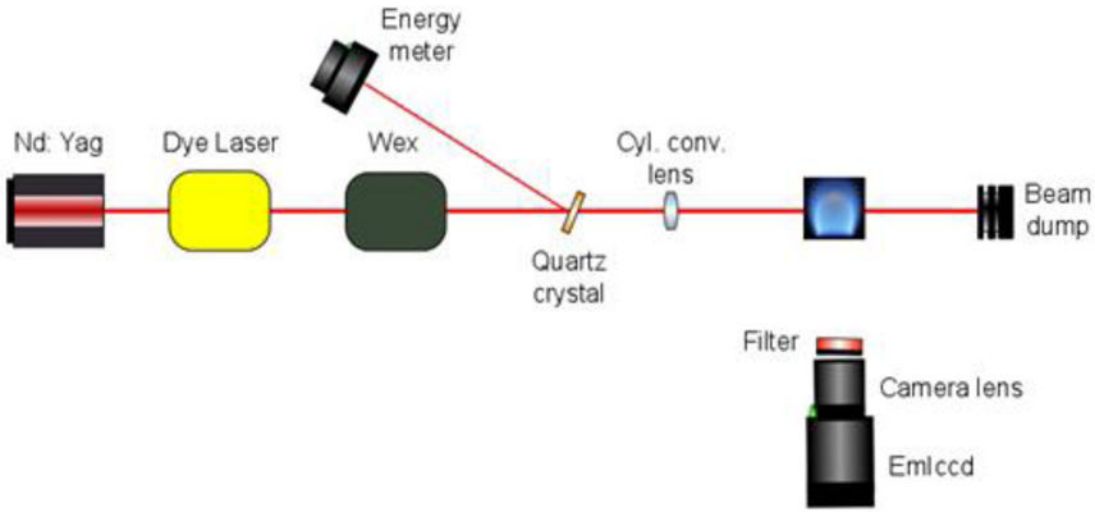

Figure 5.
Schematic of the PLIF experimental setup.

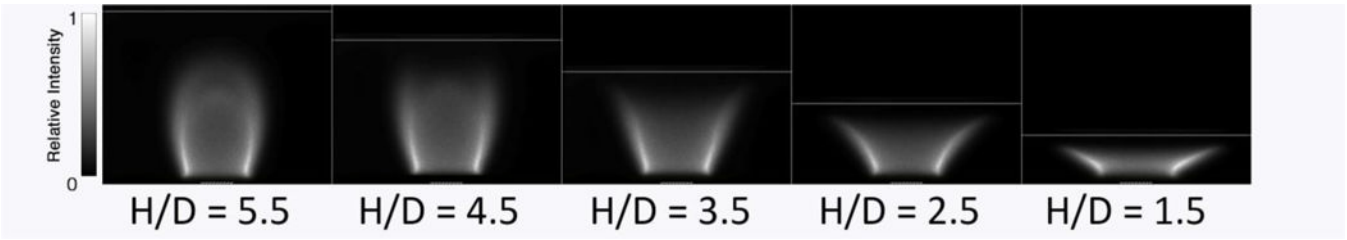

Figure 6.
OH* chemiluminescence.

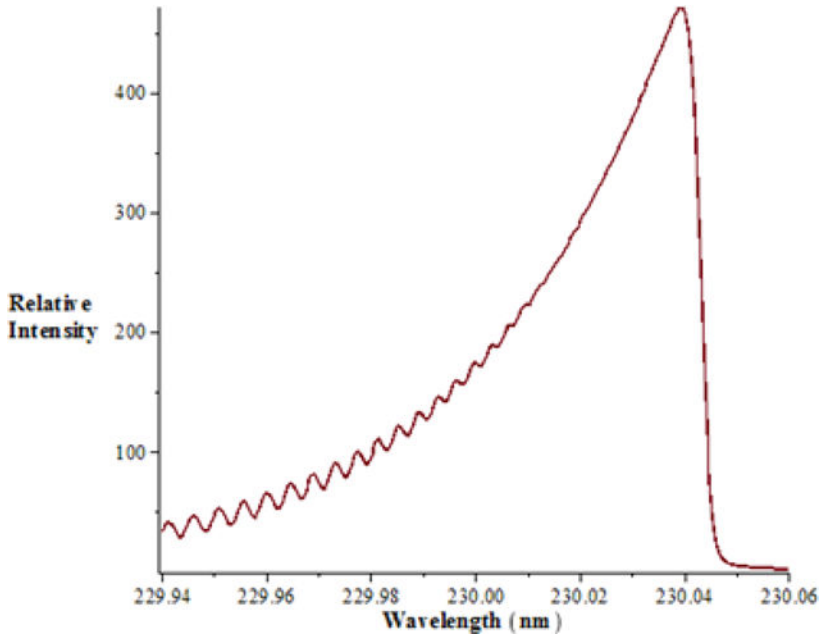

Figure 7.

Simulated fluorescence excitation spectrum for the Q branch (0,0) band of the B1Σ+←←XΣ+ transition of CO.

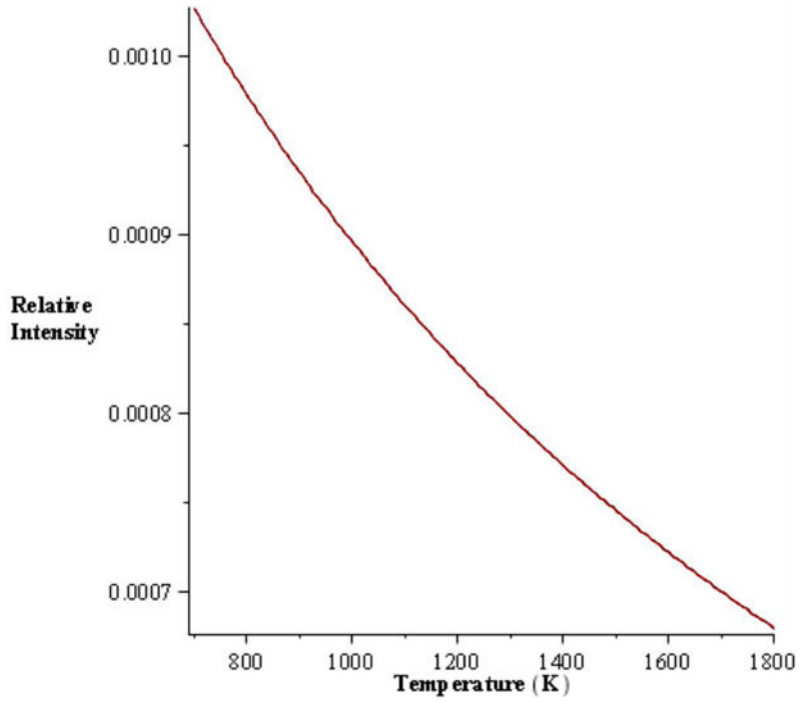

Figure 8.

Simulated temperature dependence of the fluorescence signal assuming constant number density for the Q branch (0,0) band of the B1Σ+←←XΣ+ transition of CO at the wavelength of 230.034 nm.

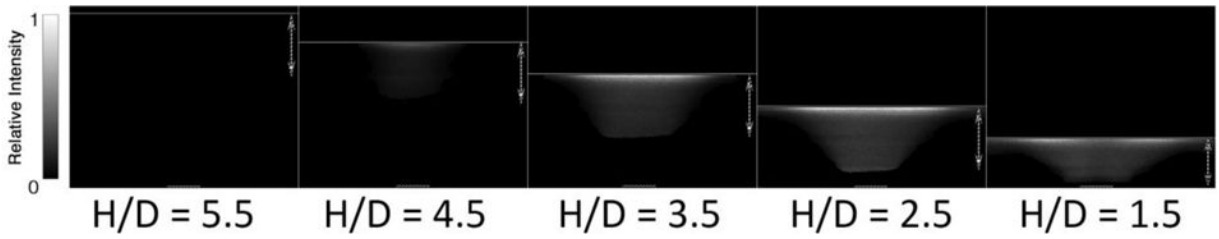

Figure 9.
Two-photon CO PLIF. The double arrow indicates the vertical extent of the laser sheet.

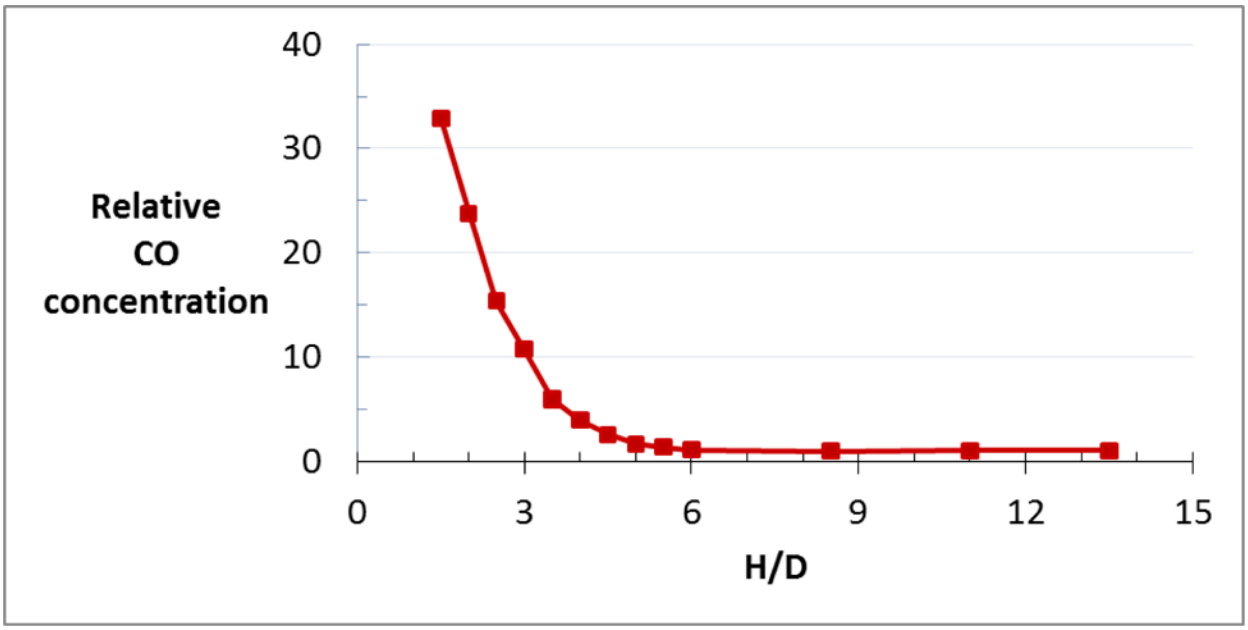

Figure 10.

CO emission changes with plate to burner distance. The absolute value of CO concentration at the asymptotic baseline condition beyond H/D of 6 is approximately 17.5 ppm.

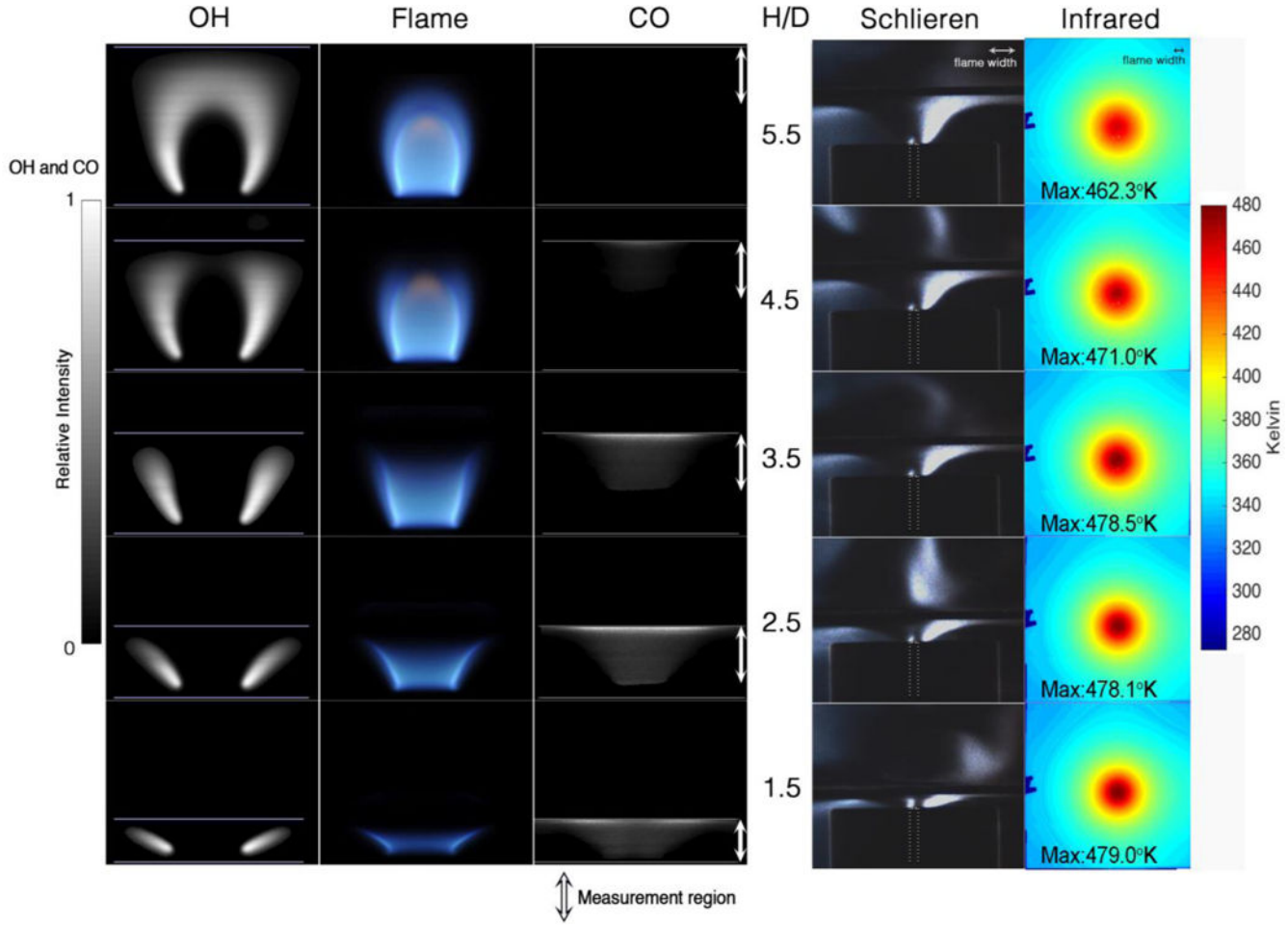

Figure 11.

The overall data at different plate heights. Note that the physical domain of the schlieren and infrared images is much larger than that of the flame focused images. A scale marker representing the approximate flame width is included on the schlieren and infrared images.

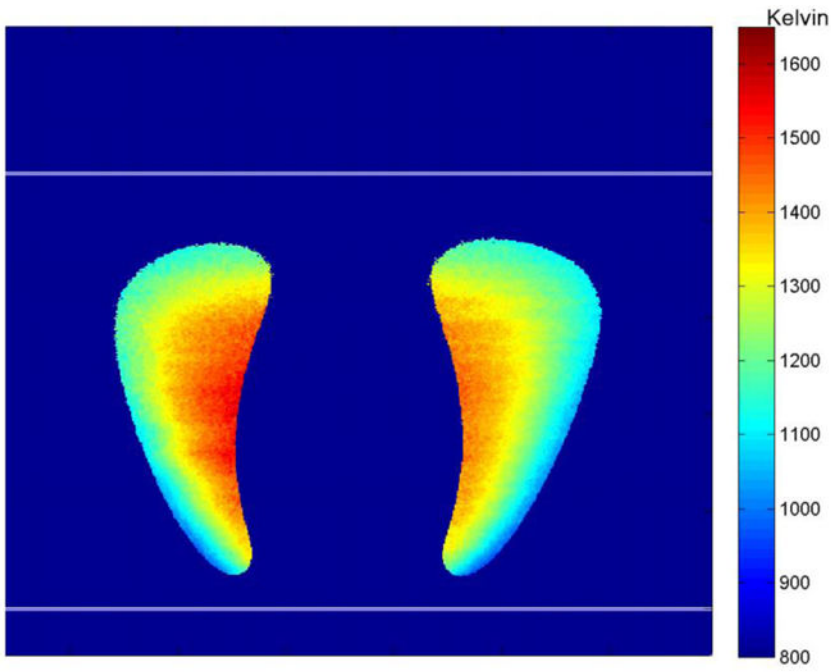

(a) H/D=4.5

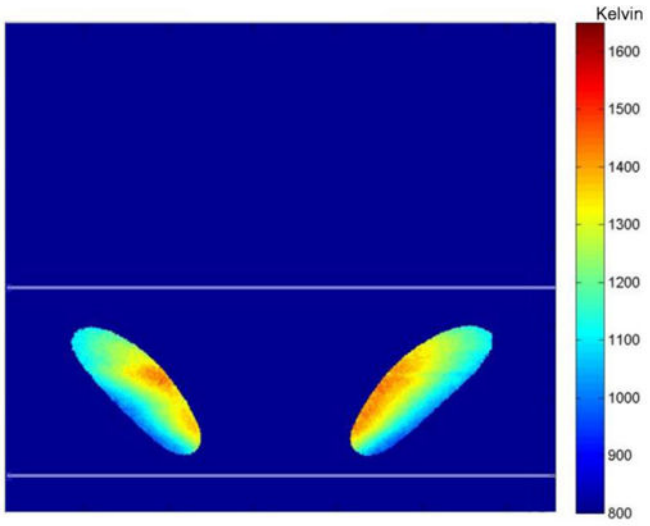

(b) H/D=2.5

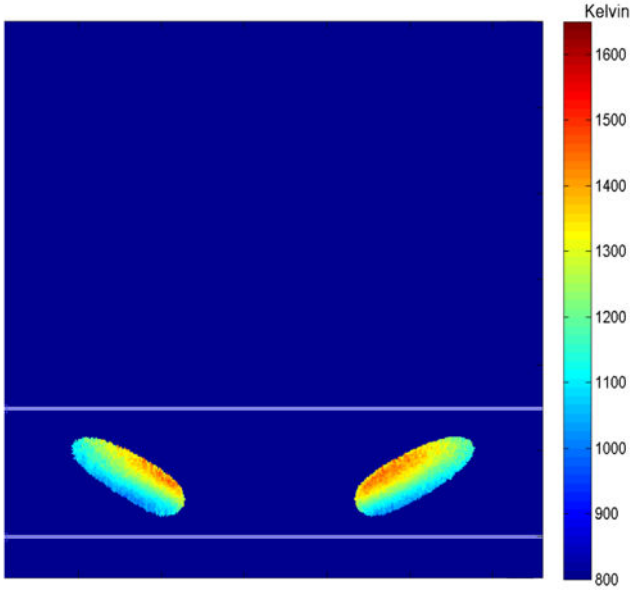

(c) H/D=1.5

Figure 12.
OH PLIF temperature measured between R1(3) and R1(10) at different plate-to-burner H/D distance.